DOI: 10.1002/ejic.200900853

Hydrothermal Synthesis of a $CaNb_2O_6$ Hierarchical Micro/Nanostructure and Its Enhanced Photocatalytic Activity

Yingwei Zhang,[a] Chao Liu,[a] Guangsheng Pang,*[a] Shihui Jiao,[a] Shiyao Zhu,[a] Dong Wang,[a] Daxin Liang,[a] and Shouhua Feng[a]

Keywords: Nanostructures / Hydrothermal synthesis / Niobium / Photocatalysis

A novel $CaNb_2O_6$ hierarchical micro/nanostructure was successfully fabricated under mild hydrothermal conditions in the absence of templates or organic additives. In this hierarchical micro/nanostructure, the nanosheets grow vertically on the surface of the one-dimensional microneedles whose axial direction is along the *c*-axis, and the single crystalline nanosheets are parallel to the (020) planes. A two-step nucleation–growth mechanism is proposed to explain the formation of the $CaNb_2O_6$ hierarchical micro/nanostructure, based on the observation of a time-dependent morphology evolution process. The hierarchically structured $CaNb_2O_6$ exhibits a stronger enhancement of photocatalytic activity in the degradation of rhodamine B (RhB) than other morphological $CaNb_2O_6$ samples, such as nanoparticles, nanoribbons, and microneedles. This simple hydrothermal method provides a new general approach for the synthesis of potentially useful niobates.

Introduction

Hierarchical micro/nanostructures, which are assembled from zero-dimensional (0D), 1D, and 2D micro/nanoscale building blocks, have attracted significant attention due to their unique physical and chemical properties.[1–4] Research on hierarchical structures provides potential applications in the bottom-up fabrication of advanced functional devices, including sensors,[5,6] fuel cells,[7] and photocatalysts.[8–10] The photocatalytic superiority of the hierarchical micro/nanostructures can be attributed to their special structural features. The special structural features can prevent aggregation to maintain a large active surface area and enhance the charge-transfer rates in materials.[8–11] So far, various hierarchical morphologies of different materials (such as core-shell,[8] tubular,[12] dendrites,[13] flower-like,[11,14] dandelion-like,[15] and brush-like[5]) have been synthesized in solution. Commonly, templates or surfactants are required in the synthesis process of hierarchical structures, in order to decrease the interfacial energy barrier for sequential nucleation–growth or to induce the self-assembly process of primary particles.[16,17]

Among all the semiconductor photocatalysts reported, a series of niobates showed high photocatalytic activity, for example $NiNb_2O_6$,[18] $ZnNb_2O_6$,[19] $SnNb_2O_6$,[20] $Cs_2Nb_4O_{11}$,[21] $Sr_2Nb_2O_7$,[22] $Ca_2Nb_2O_7$,[23] H(K)$Ca_2Nb_3O_{10}$,[24] $Ba_5Nb_4O_{15}$,[25] $K_4Nb_6O_{17}$,[26] and $InNbO_4$.[27] Although the photocatalytic activity of these niobates has been confirmed by theoretical calculation and experiments, the cumbersome synthesis conditions limited their practical applications. Currently, most niobates are synthesized by traditional solid-state reaction (SSR) and related methods, such as the polymerized complex (PC) method,[25,28] sol–gel method,[29,30] and the molten salt route.[31] The products obtained by the SSR method are generally bulk materials with low active surface area and wide size distribution.[18b,27] Because of polyesterification between citric acid and ethylene glycol in the PC and sol–gel methods, expensive Nb sources are always required, such as $NbCl_5$ and $Nb(OC_2H_5)_5$.[8,29] The final calcination process is inevitable and causes a loss of active surface area. Usually, awkward Nb_2O_5 treatments are needed, in order to obtain soluble and more reactive hydrated $Nb_2O_5{\cdot}nH_2O$, which is also called "niobic acid", for example fusing Nb_2O_5 at 400 °C with KOH and dissolving Nb_2O_5 in concentrated HF solution.[30,32] Although, there are some reports of hydrothermal synthesis under mild conditions, most of them focus on the synthesis of alkali metal niobates,[33–35] based on the dissolution of Nb_2O_5 in alkaline solutions by hydrothermal treatment.

$CaNb_2O_6$, one of the columbite niobate compounds (MNb_2O_6 where M = Mg, Zn, Ni, Ca, Cu, Mn, or Co), has received a great deal of attention due to its microwave dielectric and photocatalytic properties.[36–38] In addition, it is reported that $CaNb_2O_6$ can be used in holography applications, as a laser host material and a low-cost lamp phosphor when doped with Eu^{3+} and co-doped with Ti^{4+}.[39]

[a] College of Chemistry, State Key Laboratory of Inorganic Synthesis and Preparative Chemistry, Jilin University, Changchun, Jilin 130012, P. R. of China
Fax: +86-0431-85168624
E-mail: panggs@jlu.edu.cn

Supporting information for this article is available on the WWW under http://dx.doi.org/10.1002/ejic.200900853.

Synthetic methods of $CaNb_2O_6$ in the current literature are all limited to high-temperature calcination, the sol-gel method, and molten-salt reaction.[29,36,38,40]

In our work, based on the reaction between a more reactive Nb precursor and Ca^{2+} in a hydrothermal process, a $CaNb_2O_6$ hierarchical micro/nanostructure was obtained without templates or organic additives. We have investigated the effect of reaction conditions including pH value, reaction time, temperature, and reactant concentration on the growth and morphology of $CaNb_2O_6$ products. The corresponding optical absorption and photocatalytic activities of $CaNb_2O_6$ samples with different morphologies were also studied.

Results and Discussion

Figure 1 shows the X-ray diffraction patterns of the samples prepared by hydrothermal treatment requiring 1 d at 200 °C. $CaNb_2O_6$ and $Ca_2Nb_2O_7$ could be obtained, in different basic capacity conditions. When pH = 7 (Figure 1, a), all of the diffraction peaks could be well-indexed to a pure orthorhombic phase of $CaNb_2O_6$ (JCPDS No. 39–1392). When the pH value was increased to 8 (Figure 1, b), there was also only $CaNb_2O_6$. But as the pH value increased further, $Ca_2Nb_2O_7$ coexisted with $CaNb_2O_6$, and the diffraction peak intensity of $Ca_2Nb_2O_7$ increasingly strengthened while the diffraction peak intensity of $CaNb_2O_6$ weakened (Figure 1, c–e). At pH = 10 there is clear coexistence of $CaNb_2O_6$ and $Ca_2Nb_2O_7$, as shown in Figure 1 (d), and at pH = 11, $Ca_2Nb_2O_7$ was the main phase in the mixture products. The amount of $CaNb_2O_6$ in the mixture was 70.9, 65.9, and 44.1 wt.-% at the pH values of 9, 10, and 11, respectively, as estimated by the Rietveld software MAUD. A pure phase of $Ca_2Nb_2O_7$ could be obtained at a pH > 13. As shown in Figure 1 (f–h), all diffraction peaks of the $Ca_2Nb_2O_7$ phase are in good agreement with the standard XRD card (JCPDS No. 81-0841).

We used a soluble and active Nb^V precursor which is prepared by a relatively simple and convenient hydrothermal treatment of Nb_2O_5. Although it is the commonest and cheapest niobium source in niobium chemistry, Nb_2O_5 is fairly inert in aqueous solution. So often in the literature cumbersome techniques have been necessary to obtain soluble and more reactive hydrated $Nb_2O_5{\cdot}nH_2O$, for example fusing Nb_2O_5 with alkali metal (usually potassium) hydroxides or carbonates, and dissolving Nb_2O_5 in concentrated HF solution.[30,32] Since the hexaniobate ion $[Nb_6O_{19}]^{8-}$ has been known as the dominant species in alkaline solutions[41,42] and the solution of $[Nb_6O_{19}]^{8-}$ could be obtained by hydrothermal process,[43,44] we chose the alkali salt of $[Nb_6O_{19}]^{8-}$ as the water-soluble precursor for the synthesis of $CaNb_2O_6$. Additionally, it has been mentioned above that the pH value of the solution as well as the niobium oxide concentration determines the specific niobium ionic species present in aqueous solution,[45] for example $H_xNb_6O_{19}^{(8-x)-}$ (x = 0, 1, 2, or 3) present in the pH range 11.5–14.5, and $Nb_2O_5{\cdot}nH_2O$ which exists in aqueous solutions of pH = 3.65–6.5. So the synthesis of $CaNb_2O_6$ and $Ca_2Nb_2O_7$ can be expressed by Equations (1) or (2) for pH ≤ 8 or > 13, respectively.

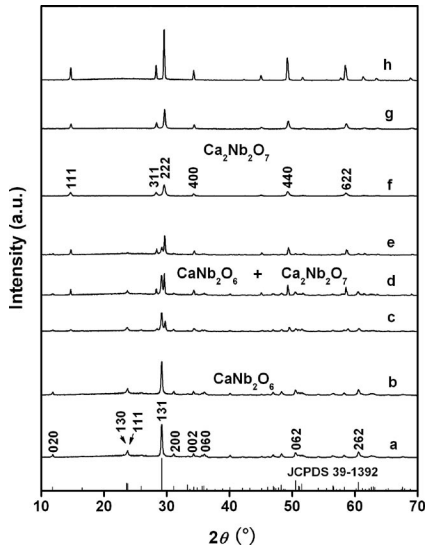

Figure 1. XRD patterns of the samples prepared by hydrothermal treatment at 200 °C for 24 h in different basic capacity conditions: (a) pH = 7, (b) pH = 8, (c) pH = 9, (d) pH = 10, (e) pH = 11, (f) 0.2 M KOH, (g) 1 M KOH, and (h) 5 M KOH.

$$Nb_2O_5{\cdot}nH_2O + Ca^{2+} \rightarrow CaNb_2O_6 + (n-1)H_2O + 2H^+ \quad (1)$$

$$H_xNb_6O_{19}^{(8-x)-} + (x+4)OH^- + 6Ca^{2+} \rightarrow 3Ca_2Nb_2O_7 + (x+2)H_2O \quad (2)$$

Figure 2 presents the typical electron microscopy images of the obtained $CaNb_2O_6$ with hierarchical structure prepared at 200 °C for 3 d. The low magnification scanning electron microscopy (SEM) image (Figure 2, a) shows that this hierarchical structure is common in the products. On the basis of further observations by SEM and TEM (Figure 2, b, c and d), the hierarchical structure seems to be composed of numerous two-dimensional nanosheets that stand vertically on the surface of the one-dimensional microneedles. In general, the microneedles are several micrometers in length, with diameters of ca. 300 nm. The secondary nanosheets are very thin and the folds of nanosheets could be clearly observed in Figure 2 (e). These nanosheets are usually flat-lying on the Cu grids, and the thickness of the nanosheet is approximately 6 nm from the width of the fold as marked in Figure 2 (e). Figure 2 (f) is a high-resolution TEM (HRTEM) image, and represents the inset rectangle at the edge of the nanosheet in Figure 2 (e). The clear lattice fringe confirms the single-crystalline nature of the nanosheet. The measured interplanar spacings are 0.287 nm and 0.260 nm, which are in good agreement with the values of the (200) and (002) lattice planes, respectively. The angle between the two fringes is very close to 90°, showing that the HRTEM is taken from the [010] zone axis. Therefore, we conclude that the single-crystalline two-dimensional $CaNb_2O_6$ nanosheets grow preferentially along the (020) planes and spread out from the microneedles. The chemical

composition of the as-synthesized $CaNb_2O_6$ with hierarchical structure was investigated using energy-dispersive spectroscopy (EDS), as shown in Figure 2 (g). The Nb, Ca, and O peaks together with a Cu signal coming from the TEM grid are clearly shown. X-ray fluorescence analysis also confirmed the composition of $CaNb_2O_6$, and no potassium impurities were detected.

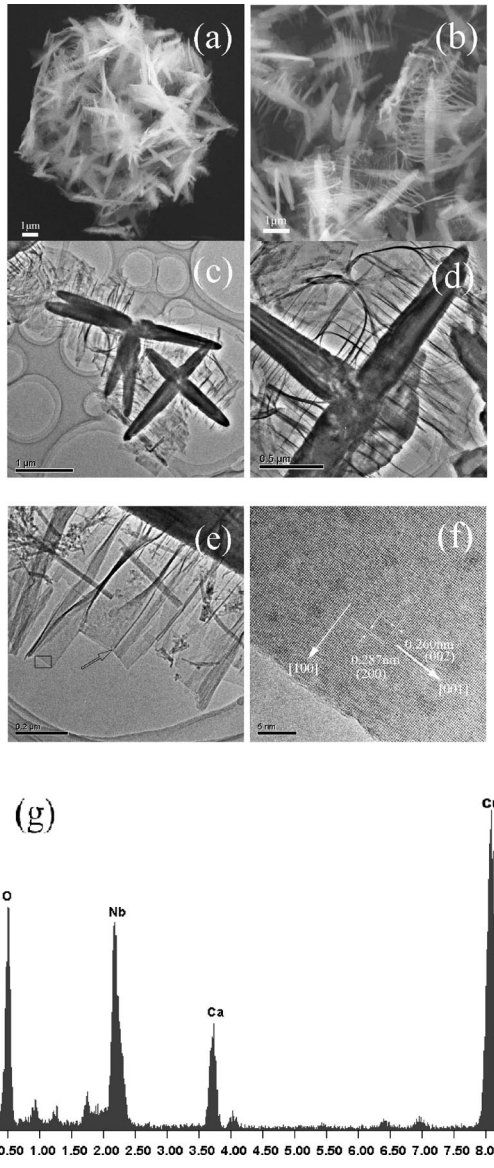

Figure 2. (a) and (b) SEM images, (c)–(e) TEM images, (f) HRTEM image recorded from the edge of a nanosheet, (g) EDS of the hierarchically structured $CaNb_2O_6$ prepared by hydrothermal treatment at 200 °C, pH = 7.2 for 3 d.

To understand how the hierarchical structure of $CaNb_2O_6$ formed, a series of time-dependent experiments were performed at 200 °C. Figure 3 shows the morphological evolution process of the samples after different reaction times. After 2 h, many tiny irregular nanoparticles were formed as the main product (Figure 3, a) and the crystalline phase of $CaNb_2O_6$ emerged (XRD pattern shown in Figure 4). At the same time, some one-dimensional microneedles could be observed occasionally, as shown in Figure 3 (b). When the reaction time was prolonged to 1 d, the irregular nanoparticles almost disappeared, and at this time the products present the morphology of one-dimensional microneedles, and many multiarmed microneedles could be observed, as shown in Figure 3 (c). A close examination of a single microneedle is shown in Figure 3 (d). The well-resolved two-dimensional lattice fringes shown in the HRTEM image indicate the single-crystalline nature and good crystallinity of the microneedle. In addition, the spacings between the two sets of fringes are determined to be 0.532 nm and 0.260 nm, which are very close to the interplanar spacings of the (110) and (002) planes, respectively, indicating that there is preferential growth of the microneedles along the [001] direction. When reaction time was further extended to 2 d, the microneedles became thicker and some nanosheets emerged, which stand nearly vertically on the surface of the microneedles as shown in Figure 3 (e). When the reaction time exceeded 3 d, the hierarchical micro/nanostructure became widespread, and the size of the nanosheets increased markedly as shown in Fig-

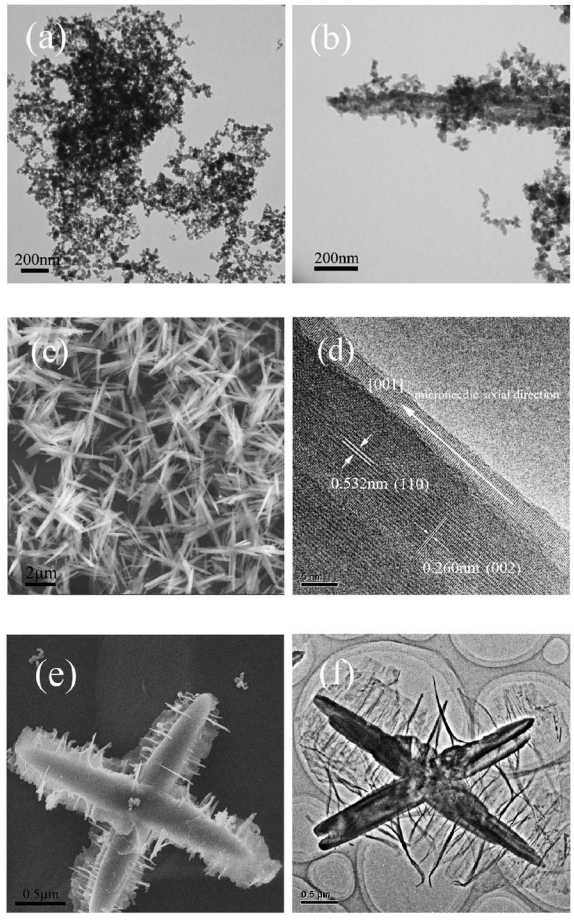

Figure 3. SEM and TEM images of $CaNb_2O_6$ samples prepared by hydrothermal treatment at 200 °C for different reaction times: (a, b) 2 h, nanoparticles and one-dimensional nanostructures aggregated by nanoparticles. (c, d) 1 d, microneedles and HRTEM image of an individual microneedle, (e) 2 d, nanosheets emerge, (f) 3 d, hierarchical micro/nanostructure.

ure 3 (f). This result indicates that $CaNb_2O_6$ microneedles with preferred growth along the [001] direction formed first, and then $CaNb_2O_6$ nanosheets grew gradually on the surface of these microneedles, leading to the formation of the $CaNb_2O_6$ hierarchical micro/nanostructure. When the reaction time was increased to 5–10 d, the nanosheets became thicker and the diameters of the microneedles increased to ca. 1 μm, as shown in Figure S1.

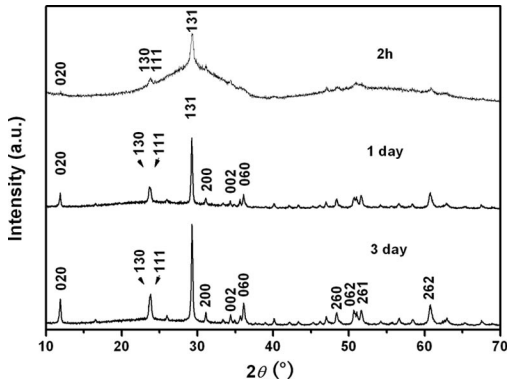

Figure 4. XRD of the $CaNb_2O_6$ samples prepared by hydrothermal treatment at 200 °C and for different reaction times.

In general, the morphology of crystal growth is determined by a combination of internal structurally related factors and external factors (such as supersaturation degree, time, and additives). As for internal structural factors, in the columbite structure of $CaNb_2O_6$ (Figure 5), NbO_6 octahedra joined together at their edges along the *c*-axis to form chains, and two adjacent chains are linked to each other at their corners. These double layers of edge- and corner-shared NbO_6 octahedra are connected into a sheet as the basic structural unit and the sheets are separated along the *b*-axis by layers of Ca^{2+} ions as interlayer counterions. Thus, it is structurally reasonable to assume that the nanosheets grown on the surface of the one-dimensional microneedles were formed from the sheet layers which are parallel to its instinct $a \times c$ layer plane, and this result is consistent with the HRTEM observation.

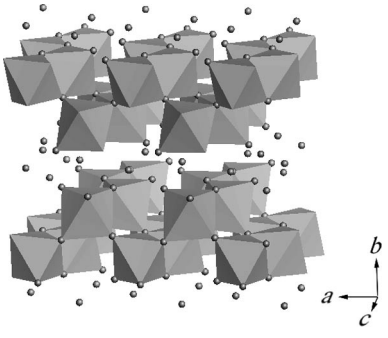

Figure 5. Crystal structure of columbite $CaNb_2O_6$. The small spheres represent Ca atoms and the octahedra represent NbO_6 octahedra.

As for external factors, we considered supersaturation degree and reaction temperature besides reaction time. Firstly, the supersaturation degree has a crucial effect on the nucleation process.[14] Only with an appropriate concentration of reactants, is the multistep nucleation–growth process feasible and can the construction of the hierarchical structure be realized. In regard to our experiments, microneedles formed in the first nucleation–growth stage could serve as substrates to induce secondary heterogeneous nucleation of the nanosheets, while the remaining concentration is sufficiently high to initiate nucleation. In order to demonstrate this, we performed an experiment over 3 d with a lower concentration of reactants (0.002 mol/L of Nb and 0.002 mol/L of Ca). The SEM images in Figure 6 (a) show that the products present the morphology of microplates and no secondary nanosheets were identified. Additionally, the morphology of the corresponding $CaNb_2O_6$ samples prepared at lower temperature for 3 d has also been studied by SEM analysis and is presented in Figure 6 (b). When reaction temperature was decreased to 180, 160, and 140 °C (XRD patterns shown in Figure 7), the products present a similar morphology of nanoribbons (Figure S2), and some nanoribbons assemble into nanoflowers as shown in Figure 6 (b), but there is no secondary nanostructure. The thickness of the nanoribbons is 27 nm, and that is smaller than the microneedles prepared at 200 °C.

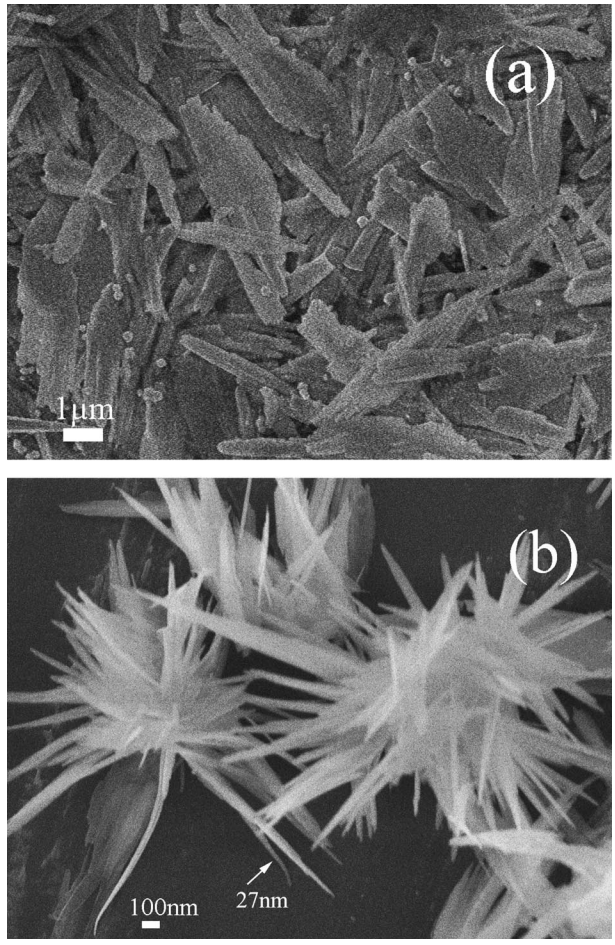

Figure 6. SEM of $CaNb_2O_6$ samples prepared by hydrothermal treatment for 3 d at lower concentration and reaction temperature, (a) 0.002 mol/L of Nb and 0.002 mol/L of Ca, (b) 160 °C.

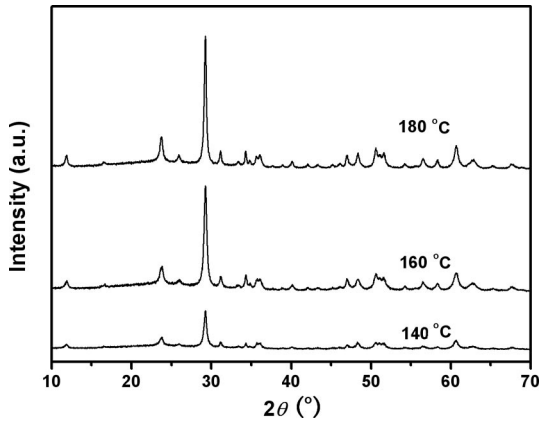

Figure 7. XRD patterns of $CaNb_2O_6$ samples prepared at different reaction temperature for 3 d.

On the basis of the above observations and discussion, we believe that the hierarchical structure is formed in a two-step nucleation–growth process, at appropriate concentration and temperature conditions. The whole process is demonstrated in Scheme 1. During the first step (Scheme 1, a), a lot of tiny crystalline nuclei particles were formed after hydrothermal treatment for 2 h, and some microneedles that were aggregations of tiny particles appeared. Larger microneedles grew at the cost of the small particles based on an Ostwald ripening mechanism. Finally, the irregular nanoparticles almost disappeared when reaction time further increased to 1 d. The growth direction of the microneedles is derived from the intrinsic anisotropic growth habit. In the second step (Scheme 1, b), surplus crystal seeds initiated secondary heterogeneous nucleation on the surface of the microneedles, resulting in secondary nanosheets growing on the surface of the $CaNb_2O_6$ microneedles and a hierarchical structure is formed. The fact that there are no hierarchical structures at lower concentrations provided distinct evidence that the supersaturation degree is crucial to the construction of the hierarchical structure. Currently, a sequential nucleation–growth strategy has been successfully employed to construct hierarchical structures in many systems. However, preformed primary nanocrystals and the assistance of organic additives to reduce the interfacial activation energy and induce the site-specific nucleation–growth process on the surfaces of primary nanocrystals are necessary.[17] Comparatively speaking, our result may provide a new route for the construction of such a hierarchical structure from a multistep nucleation–growth process dependent on the degree of supersaturation.

Figure 8 shows the UV/Vis diffuse reflectance spectra of the $CaNb_2O_6$ products. All of the samples exhibited absorption bands in the UV light region, and the band gaps of $CaNb_2O_6$ are estimated according to the absorption edge position from the interception of the two linearly extrapolated lines as shown in part d of Figure 8. Figure 8 (a–c) shows that the optical absorption edge positions of the $CaNb_2O_6$ products prepared at 200 °C are ca. 345 nm, corresponding to a band-gap energy of 3.59 eV. It is observed that the optical absorption edge of $CaNb_2O_6$ nanoribbons prepared at 160 °C is ca. 333 nm (Figure 8, d), corresponding to a band-gap energy of 3.75 eV. The length, width, and especially thickness (27 nm) of the nanoribbons is less than the microneedles prepared at 200 °C. The optical absorption of the product prepared at 160 °C exhibits a slight blue shift, compared to the samples obtained at 200 °C. Figure 8 (e) shows the UV/Vis diffuse reflectance spectra of $CaNb_2O_6$ prepared by a conventional SSR. The optical absorption of the SSR-$CaNb_2O_6$ sample presents a negative absorption value in the shorter wavelength region, which is probably due to the strong luminescence property of the SSR-$CaNb_2O_6$ sample at room temperature.[38,39] The shape and structure could have an effect on the optical absorption and band-gap energy[46,47] and the differences in optical absorption of the different samples were ascribed to that.

The photocatalytic activities of $CaNb_2O_6$ products were evaluated by decomposition of RhB in aqueous solution. As shown in Figure S3, when a $CaNb_2O_6$ hierarchical micro/nanostructure sample is suspended in the RhB solution, the absorption of the RhB dye solution decreased

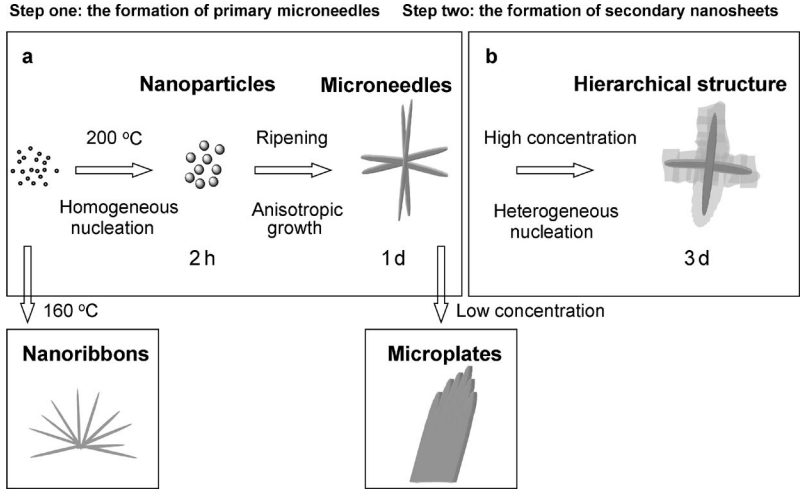

Scheme 1. Illustration of the two-step nucleation–growth process for the formation of the $CaNb_2O_6$ hierarchical micro/nanostructure.

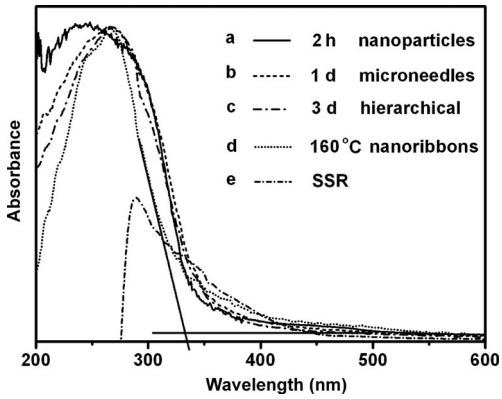

Figure 8. UV/Vis diffuse reflectance spectrum of $CaNb_2O_6$ products with different morphologies: (a) nanoparticles, (b) microneedles, (c) hierarchical structural morphology, (d) nanoribbons, (e) SSR-$CaNb_2O_6$.

gradually under UV light irradiation and the major absorption peak position was slightly blue shifted, indicating degradation of the RhB and removal of ethyl groups. A series of photocatalytic experimental results are shown in Figure 9. The *y*-axis was defined as C/C_0, where C is the absorption of RhB at irradiation time t, and C_0 is the absorption of RhB after the adsorption equilibrium. A blank test (RhB without any catalyst) under 500-W UV light radiation was performed and is shown in Figure 9 (a); the test revealed that the degradation of RhB was very slow when illuminated by UV light in the absence of photocatalysts. However, with $CaNb_2O_6$ samples as photocatalysts, the photodegradation efficiencies of RhB clearly increased. The $CaNb_2O_6$ hierarchical micro/nanostructured morphology showed the highest photocatalytic activity (Figure 9, f), followed by nanoribbons prepared at 160 °C (Figure 9, e), microneedles (Figure 9, d), and nanoparticles (Figure 9, c). All the hydrothermally treated samples have better photocatalytic activity than the SSR-$CaNb_2O_6$ sample (Figure 9, b).

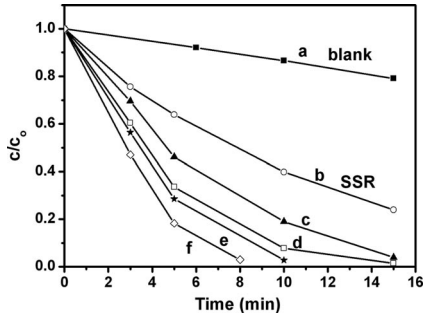

Figure 9. Photocatalytic degradation of RhB using different $CaNb_2O_6$ samples: (a) without photocatalysts under UV light irradiation, (b) SSR-$CaNb_2O_6$, (c) nanoparticles, (d) microneedles, (e) nanoribbons, (f) hierarchical micro/nanostructure.

Before the irradiation with UV light, the adsorption percentages of RhB in different samples were checked. Table S1 shows the BET surface areas and the adsorption percentages of RhB for different morphological $CaNb_2O_6$ photocatalysts in the dark. The photocatalytic activity is related to the surface area of the photocatalyst, and the improved activity is usually accompanied with an increase in surface area. However, in our experiments, the nanoparticles (BET = 91 m^2/g) with higher surface area, as well as the nanoribbons (BET = 43.5 m^2/g), exhibit lower photocatalytic activity than the hierarchical micro/nanostructural sample (BET = 23.5 m^2/g). The SSR sample (BET = 1.7 m^2/g) shows the lowest photocatalytic activity. The differences in crystallinity and the special structural morphology are responsible for this. Nanoparticles with the highest BET surfaces were obtained at 2 h but the crystallinity was poor, so the increased number of defects may act as recombination centers for photoinduced electrons and holes, and reduce the photocatalytic activity significantly. In addition, regarding other samples with similar crystallinity and the same energy band structure, differences in photocatalytic activity could be ascribed to differences in morphology and micro/nanostructures, which affect the efficiency of the electron–hole separation. The unique structure of the hierarchical micro/nanostructured $CaNb_2O_6$ may be responsible for its highest photocatalytic activity. The thickness of secondary nanosheets that grow vertically on the surface of the one-dimensional microneedles is ca. 6 nm, and this will promote transfer of the photogenerated charge carriers from the inside to the surface of the crystal where they react with the organic molecules.[48] As a matter of fact, the thickness of 6 nm is very close to the regime where quantum size effect is prominent. The quantum size effects would induce the broadening of the nanosheets' band gap and bring higher redox potentials. The electrons transferring from the conductive bands of nanosheets with high electric potential to those of the microneedles with low electric potential could be promoted. The recombination probability of the photogenerated electron–hole pair could be reduced, and then the efficiency of the electron–hole separation increased.[8,49] Therefore, a good photocatalytic performance is obtained. However, the detailed carrier charge-transfer processes and reactions in $CaNb_2O_6$ hierarchical micro/nanostructures still require further investigation.

Conclusions

Starting from the inert but cheapest niobium source in niobium chemistry, Nb_2O_5, a $CaNb_2O_6$ hierarchical micro/nanostructure was synthesized for the first time by a simple hydrothermal reaction without templates. At the same time, selective synthesis of $CaNb_2O_6$ and $Ca_2Nb_2O_7$ could also be facilely achieved only by adjusting pH value. This simple and low-cost hydrothermal method may also be extended to prepare other similarly structured niobates and such studies are in progress. The $CaNb_2O_6$ hierarchical structure shows nanosheets standing vertically on the surface of the microneedles. The structural features of the $CaNb_2O_6$ hierarchical micro/nanostructure could efficiently promote the charge-transfer process and lead to a good photocatalytic performance in the decomposition of RhB under UV light irradiation. The formation of this hierarchical micro/nano-

structure can be described by a two-step nucleation–growth process. First of all, primary microneedles form in the first nucleation–growth stage, and then, these microneedles serve as substrates to induce heterogeneous nucleation of the secondary nanosheets. Ultimately, the hierarchical morphology can be achieved with appropriate time and temperature conditions, especially if the supersaturation degree required by the multistep nucleation–growth process is high enough. The comprehension of this multistep nucleation–growth process could be useful in the construction of new hierarchical structures with potential uses.

Experimental Section

Synthesis of a Soluble Niobium Source: Niobium pentaoxide (Nb_2O_5, 0.5 g) and KOH (1 M) alkaline solution were mixed and transferred into a 40 mL Teflon®-lined stainless steel autoclave. Thermal treatment was carried out at 180 °C for 2 d. After cooling down naturally, any insoluble residue was eliminated by centrifuging. The clear colorless solution of $[Nb_6O_{19}]^{8-}$ was obtained, according to the literature.[43,44]

Synthesis of Calcium Niobate Samples: In a typical procedure, the above solution (2 mL) was taken and diluted in distilled water (13 mL). Hydrochloric acid was used to adjust the pH value of the solution to 7.2, then $CaCl_2$ (15 mL, 0.017 M) was added under continuous stirring. The pH value of the solution was adjusted again to 7.2. The mixture (30 mL) was transferred into a 40 mL Teflon-lined stainless steel autoclave. The autoclave was heated at 200 °C for 3 d and then cooled down naturally. The products were filtered, washed with distilled water, and dried in a vacuum at 60 °C for 12 h. The morphology of this product was observed to be that of the hierarchical micro/nanostructure. A series of experiments involving changing the pH value from 7 to 13 were also performed at 200 °C for 1 d.

For comparison, a $CaNb_2O_6$ sample was also prepared by SSR. $CaCO_3$ (0.2 g) and Nb_2O_5 (0.532 g) with a required stoichiometry were mixed and milled, and then the powder was pressed into a pellet. The pellet was heated in an alumina crucible at 850 °C for 12 h, and then at 1300 °C for 12 h twice with regrinding.

Characterization: The XRD patterns of the products were obtained with a Rigaku D/MAX 2500/PC X-ray diffractometer with graphite-filtered Cu-K_α radiation, at 40 kV and 200 mA, and collected at 2θ angles of 10–70°. The morphologies of the samples were observed by SEM on a JSM-6700F electron microscope and TEM on a JSM-3010 electron microscope. The UV/Vis diffuse reflectance spectrum of the products was obtained with the Lambda 20 UV/Vis spectrometer. The BET surface areas of the samples were measured with a Micromeritics Tristar 3000 system. The chemical compositions of prepared samples were verified using X-ray fluorescence (XRF) with a Panalytical AXIOS PW4400 sequential spectrophotometer.

Measurement of Photocatalytic Activity: The photocatalytic activities of samples were evaluated by the photocatalytic degradation of RhB under UV light. A 500-W high-pressure Hg lamp was used as the UV light source. Experiments were carried out at ambient temperature as follows: a catalyst (10 mg) was suspended in a RhB solution (100 mL, 10^{-5} mol/L). Before illumination, the aqueous suspension was stirred for 1 h in the dark to ensure adsorption–desorption equilibrium. Then, the suspension was exposed to UV light irradiation under continuous stirring. The concentrations of the RhB were monitored by measuring the absorbance of the solution at 553 nm during the photodegradation process with a UV-2450 UV/Vis spectrophotometer.

Supporting Information (see also the footnote on the first page of this article): TEM characterizations of $CaNb_2O_6$ samples prepared under different conditions. Changes of UV-visible spectra of a typical $CaNb_2O_6$ hierarchical structure sample suspended in RhB solution as a function of irradiation time. BET surface area and the adsorption percentages of RhB for different morphological $CaNb_2O_6$ photocatalysts.

Acknowledgments

This research was supported by the National Natural Science Foundation of China (grant numbers 20671039 and 20121103).

[1] a) D. F. Zhang, L. D. Sun, C. J. Jia, Z. G. Yan, L. P. You, C. H. Yan, *J. Am. Chem. Soc.* **2005**, *127*, 13492–13493; b) C. V. G. Reddy, W. Cao, O. K. Tan, W. Zhu, *Sens. Actuators B* **2002**, *81*, 170–175.
[2] a) R. Ostermann, D. Li, Y. D. Yin, J. T. McCann, Y. N. Xia, *Nano Lett.* **2006**, *6*, 1297–1302; b) J. Y. Lao, J. G. Wen, Z. F. Ren, *Nano Lett.* **2002**, *2*, 1287–1291.
[3] X. F. Duan, Y. Huang, Y. Cui, J. F. Wang, C. M. Lieber, *Nature* **2001**, *409*, 66–69.
[4] X. F. Gao, L. Jiang, *Nature* **2004**, *432*, 36.
[5] Y. Zhang, J. Q. Xu, Q. Xiang, H. Li, Q. Y. Pan, P. C. Xu, *J. Phys. Chem. C* **2009**, *113*, 3430–3435.
[6] L. P. Qin, J. Q. Xu, X. W. Dong, Q. Y. Pan, Z. X. Cheng, Q. Xiang, F. Li, *Nanotechnology* **2008**, *19*, 185705.
[7] S. S. Madhu, R. Y. Li, M. Cai, X. L. Sun, *J. Power Sources* **2008**, *185*, 1079–1085.
[8] F. Lu, W. P. Cai, Y. G. Zhang, *Adv. Funct. Mater.* **2008**, *18*, 1047–1056.
[9] J. G. Yu, Y. R. Su, B. Cheng, *Adv. Funct. Mater.* **2007**, *17*, 1984–1990.
[10] L. Liu, H. J. Liu, Y. P. Zhao, *Environ. Sci. Technol.* **2008**, *42*, 2342–2348.
[11] L. Zheng, Y. Xu, Y. Song, C. Z. Wu, M. Zhang, Y. Xie, *Inorg. Chem.* **2009**, *48*, 4003–4009.
[12] C. Z. Wu, L. Y. Lei, X. Zhu, J. L. Yang, Y. Xie, *Small* **2007**, *3*, 1518–1522.
[13] L. P. Zhu, H. M. Xiao, W. D. Zhang, Y. Yang, S. Y. Fu, *Cryst. Growth Des.* **2008**, *8*, 1113–1118.
[14] D. F. Zhang, L. D. Sun, J. Zhang, Z. G. Yan, C. H. Yan, *Cryst. Growth Des.* **2008**, *8*, 3609–3615.
[15] a) B. Liu, H. C. Zeng, *J. Am. Chem. Soc.* **2004**, *126*, 8124–8125; b) B. Liu, H. C. Zeng, *J. Am. Chem. Soc.* **2004**, *126*, 16744–16746.
[16] a) H. Xue, Z. H. Li, H. Dong, L. Wu, X. X. Wang, X. Z. Fu, *Cryst. Growth Des.* **2008**, *8*, 4469–4475; b) M. H. Yu, H. N. Wang, X. F. Zhou, P. Yuan, C. H. Yu, *J. Am. Chem. Soc.* **2007**, *129*, 14576–14577.
[17] a) T. R. Zhang, W. J. Dong, M. Keeter-Brewer, S. Konar, R. N. Njabon, Z. R. Tian, *J. Am. Chem. Soc.* **2006**, *128*, 10960–10968; b) T. L. Sounart, J. Liu, J. A. Voigt, M. Huo, E. D. Spoerke, B. McKenzie, *J. Am. Chem. Soc.* **2007**, *129*, 15786–15793.
[18] a) F. E. Osterloh, *Chem. Mater.* **2008**, *20*, 35–54; b) J. H. Ye, Z. G. Zou, A. Matsushita, *Int. J. Hydrogen Energy* **2003**, *28*, 651–655.
[19] A. Kudo, S. Nakagawa, H. Kato, *Chem. Lett.* **1999**, *11*, 1197–1198.
[20] Y. Hosogi, H. Kato, A. Kudo, *Chem. Lett.* **2006**, *35*, 578–579.
[21] Y. Miseki, H. Kato, A. Kudo, *Chem. Lett.* **2005**, *34*, 54–55.
[22] a) H. G. Kim, D. W. Hwang, J. Kim, Y. G. Kim, J. S. Lee, *Chem. Commun.* **1999**, 1077–1078; b) A. Kudo, H. Kato, S. Nakagawa, *J. Phys. Chem. B* **2000**, *104*, 571–575.

[23] L. W. Zhang, H. B. Fu, C. Zhang, Y. F. Zhu, *J. Phys. Chem. C* **2008**, *112*, 3126–3133.
[24] a) H. Hata, Y. Kobayashi, V. Bojan, W. J. Youngblood, T. E. Mallouk, *Nano Lett.* **2008**, *8*, 794–799; b) K. Maeda, T. E. Mallouk, *J. Mater. Chem.* **2009**, *19*, 4813–4818; c) O. C. Compton, E. C. Carroll, J. Y. Kim, D. S. Larsen, F. E. Osterloh, *J. Phys. Chem. C* **2007**, *111*, 14589–14592; d) E. C. Carroll, O. C. Compton, D. Madsen, F. E. Osterloh, D. S. Larsen, *J. Phys. Chem. C* **2008**, *112*, 2394–2403; e) O. C. Compton, C. H. Mullet, S. Chiang, F. E. Osterloh, *J. Phys. Chem. C* **2008**, *112*, 6202–6208.
[25] Y. Miseki, H. Kato, A. Kudo, *Chem. Lett.* **2006**, *35*, 1052–1053.
[26] a) K. Maeda, M. Eguchi, W. J. Youngblood, T. E. Mallouk, *Chem. Mater.* **2008**, *20*, 6770–6778; b) R. Ma, Y. Kobayashi, W. J. Youngblood, T. E. Mallouk, *J. Mater. Chem.* **2008**, *18*, 5982–5985; c) K. Sayama, A. Tanaka, K. Domen, K. Maruya, T. Onishi, *J. Phys. Chem.* **1991**, *95*, 1345–1348.
[27] a) Z. G. Zou, H. Arakawa, *J. Photochem. Photobiol. A: Chem.* **2003**, *158*, 145–162; b) Z. G. Zou, J. H. Ye, H. Arakawa, *Mater. Res. Bull.* **2001**, *36*, 1185–1193.
[28] a) M. Yoshino, M. Kakihana, *Chem. Mater.* **2002**, *14*, 3369–3376; b) I. Pribošič, D. Makovec, M. Drofenik, *Chem. Mater.* **2005**, *17*, 2953–2958.
[29] Y. J. Hsiaoa, C. W. Liua, B. T. Daia, Y. H. Chang, *J. Alloys Compd.* **2009**, *475*, 698–701.
[30] Y. Y. Zhou, Z. F. Qiu, M. K. Lu, Q. Ma, A. Y. Zhang, G. J. Zhou, H. P. Zhang, Z. S. Yang, *J. Phys. Chem. C* **2007**, *111*, 10190–10193.
[31] B. Brahmaroutu, G. L. Messing, S. Trolier-McKinstry, *J. Am. Ceram. Soc.* **1999**, *82*, 1565–1568.
[32] B. T. Lin, J. F. Ma, Y. Yao, J. Liu, Y. Ren, X. H. Jiang, Y. Sun, Z. S. Liu, *J. Am. Ceram. Soc.* **2008**, *91*, 1329–1331.
[33] C. Sun, X. R. Xing, J. Chen, J. X. Deng, L. Li, R. B. Yu, L. J. Qiao, G. R. Liu, *Eur. J. Inorg. Chem.* **2007**, 1884–1888.
[34] A. Magrez, E. Vasco, J. W. Seo, C. Dieker, N. Setter, L. Forro, *J. Phys. Chem. B* **2006**, *110*, 58–61.
[35] a) H. Y. Zhu, Z. F. Zheng, X. P. Gao, Y. N. Huang, Z. M. Yan, J. Zou, H. M. Yin, Q. D. Zou, S. H. Kable, J. C. Zhao, Y. F. Xi, W. N. Martens, R. L. Frost, *J. Am. Chem. Soc.* **2006**, *128*, 2373–2384; b) H. W. Xu, M. Nyman, T. M. Nenoff, A. Navrotsky, *Chem. Mater.* **2004**, *16*, 2034–2040.
[36] a) R. C. Pullar, J. D. Breeze, *J. Am. Ceram. Soc.* **2005**, *88*, 2466–2471; b) H. J. Lee, K. S. Hong, S. Kim, *J. Mater. Res. Bull.* **1997**, *32*, 847–855.
[37] H. Z. An, C. Wang, T. M. Wang, W. C. Hao, *Int. J. Inorg. Mater.* **2007**, *22*, 922–926.
[38] I. S. Cho, S. T. Bae, D. K. Yim, D. W. Kim, K. S. Hong, *J. Am. Ceram. Soc.* **2009**, *92*, 506–510.
[39] a) A. A. Ballman, S. P. S. Porto, A. Yariv, *J. Appl. Phys.* **1963**, *34*, 3155–3156; b) D. Van der Voort, J. M. E. De Ruk, G. Blasse, *Phys. Status Solidi A* **1993**, *135*,621–626.
[40] C. Y. Xu, L. Zhen, R. S. Yang, Z. L. Wang, *J. Am. Chem. Soc.* **2007**, *129*, 15444–15445.
[41] a) A. Goiffon, B. Spinner, *Rev. Chim. Miner.* **1974**, *11*, 262–268; b) A. Goiffon, *Rev. Chim. Miner.* **1973**, *10*, 487–502.
[42] a) M. Nyman, T. M. Alam, F. Bonhomme, M. Rodriguez, C. Frazer, M. Welk, *J. Cluster Sci.* **2006**, *17*,197–219; b) J. R. Black, M. Nyman, W. H. Casey, *J. Am. Chem. Soc.* **2006**, *128*, 14712–14720.
[43] I. C. M. S. Santos, L. H. Loureiro, M. F. P. Silva, M. V. Cavaleiro, *Polyhedron* **2002**, *21*, 2009–2015.
[44] C. H. Lu, S. Y. Lo, H. C. Lin, *Mater. Lett.* **1998**, *34*, 172–176.
[45] I. Nowak, M. Ziolek, *Chem. Rev.* **1999**, *99*, 3603–3624.
[46] L. Zhang, W. Wang, L. Zhou, H. Xu, *Small* **2007**, *3*, 1618–1625.
[47] I. S. Cho, D. W. Kim, S. Lee, C. H. Kwak, S. T. Bae, J. H. Noh, S. H. Yoon, H. S. Jung, D. W. Kim, K. S. Hong, *Adv. Funct. Mater.* **2008**, *18*, 2154–2162.
[48] C. Zhang, Y. F. Zhu, *Chem. Mater.* **2005**, *17*, 3537–3545.
[49] C. H. Ye, Y. Bando, G. Z. Shen, D. Golberg, *J. Phys. Chem. B* **2006**, *110*, 15146–15151.

Received: August 30, 2009
Published Online: February 10, 2010

